Journal of Solid State Electrochemistry (2022) 26:1303–1311
https://doi.org/10.1007/s10008-022-05167-1

ORIGINAL PAPER

$Sr_3Mn_2O_6$ and Sr_3FeMnO_6 for oxygen and hydrogen evolution electrocatalysis

Surendra B. Karki[1] · Ram Krishna Hona[1,2] · Farshid Ramezanipour[1]

Received: 24 December 2021 / Revised: 31 March 2022 / Accepted: 1 April 2022 / Published online: 19 April 2022

Abstract

Quasi-two-dimensional oxides $Sr_3Mn_2O_6$ and Sr_3FeMnO_6 have been synthesized and their bifunctional electrocatalytic activity toward both half-reactions of water-splitting, i.e., oxygen-evolution reaction (OER) and hydrogen-evolution reaction (HER), has been demonstrated. The two materials are isostructural and consist of $(Fe/Mn)O_5$ square-pyramidal units that form two-dimensional layers, separated by strontium ions. This structure type is related to the so-called Ruddlesden-Popper (RP) structure, which typically contains 7 oxygens per formula unit and consists of octahedrally coordinated transition metals. The two materials in this work can be described as oxygen-deficient RP systems. Both compounds show electrocatalytic activity for OER and HER, with Sr_3FeMnO_6 having a significantly greater performance compared to $Sr_3Mn_2O_6$. The overpotential required for both OER and HER is considerably lowered for Sr_3FeMnO_6. This material also shows faster reaction kinetics and greater electrochemically active surface area compared to $Sr_3Mn_2O_6$. While the activity of Sr_3FeMnO_6 does not reach those of state-of-the-art catalysts, its bifunctional electrocatalytic performance is remarkable. In addition, it demonstrates the important role of electronegativity in directing functional properties such as electrocatalysis.

Keywords Solid-state structures · Water splitting · Oxygen-evolution reaction · Hydrogen-evolution reaction · Transition metal oxide

Introduction

The development of new functional oxide materials is important given their applications in different fields, such as solid oxide fuel cells (SOFCs) [1], oxygen sensors [2], and electrocatalysis [3, 4]. In particular, oxides with perovskite-related structure have received much attention due to their diverse range of properties [5, 6]. In addition, they can form several different structure types due to the possibility of oxygen removal [7] that is used to promote various properties, such as oxygen diffusivity and surface exchange kinetics at intermediate temperatures [8, 9]. There are also layered structures related to perovskites, such as Ruddlesden-Popper type structure, which has shown interesting properties, such as electrocatalysis [10]. In 1950s, Ruddlesden and Popper explored a series of oxide compounds with this type of layered structure, including those with the composition, $Sr_{n+1}Ti_nO_{3n+1}$ ($n = 1$, 2, and 3) [11, 12]. The Ruddlesden-Popper oxides can be represented by the general formula, $A_{n+1}B_nO_{3n+1}$ ($n = 1$, 2, 3…), where A represents a rare-earth or alkaline-earth metal and B is usually a transition metal. The general formula can also be expressed as $(AO)\cdot(ABO_3)_n$, where n perovskite (ABO_3) layers are sandwiched between AO rock-salt layers along the crystallographic c-axis. The simplest member of the series, A_2BO_4 ($n = 1$), adopts the K_2NiF_4 structure [13]. Other Ruddlesden-Popper phases can be realized when the thickness of perovskite stacks is increased to $n = 2$ ($A_3B_2O_7$), $n = 3$ ($A_4B_3O_{10}$), etc. As n increases from 1 to infinity (∞), the structure transitions from two-dimensional RP to three-dimensional perovskite structure, with $n = \infty$ representing a simple perovskite phase (ABO_3) [10]. The crystal structure for a typical $n = 2$ Ruddlesden-Popper oxide ($A_3B_2O_7$) is shown in Fig. 1b. Some examples of such compounds are

Surendra B. Karki and Ram Krishna Hona contributed equally to this work.

✉ Farshid Ramezanipour
farshid.ramezanipour@louisville.edu

[1] Department of Chemistry, University of Louisville, Louisville, KY 40292, USA

[2] Department of Tribal Environmental Science, United Tribes Technical College, Bismarck, ND, USA

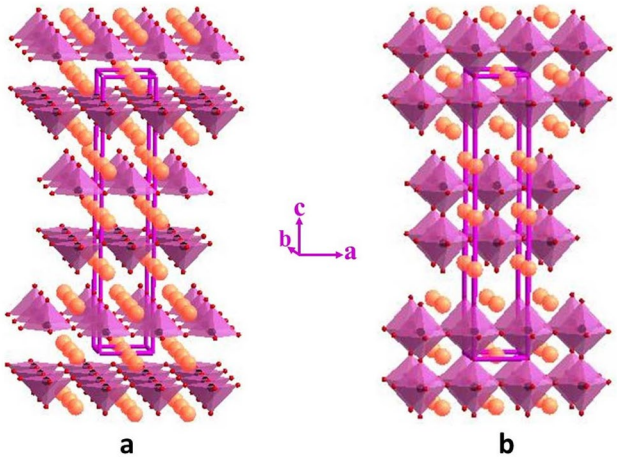

Fig. 1 **a** Crystal structure of $Sr_3Mn_2O_6$ and Sr_3FeMnO_6. The (Fe/Mn)O_5 square-pyramids are shown in purple and Sr atoms are in orange. **b** Typical Ruddlesden-Popper structure is shown for comparison

$Sr_3Fe_2O_7$ [14] and Sr_3MnO_7 [15]. It is possible to remove some of the oxygen atoms of the perovskite slabs, which will lower the coordination number of the transition metal. For example, partial reduction of $Sr_3Fe_2O_7$ transforms the FeO_6 octahedra into square pyramids [14, 16]. This indicates the structural versatility of Ruddlesden-Popper compounds, making them suitable for different applications, including electrocatalysis [10].

Among electrocatalytic processes, where Ruddlesden-Popper oxides can be utilized, is water-splitting [17], which involves two half-reactions, oxygen evolution reaction (OER), and hydrogen evolution reaction (HER). However, both OER and HER are kinetically slow and require considerable overpotentials (η). To minimize the overpotential and increase the efficiency of these processes, various catalysts, including different oxides, have been used [18, 19]. There are multiple examples of Ruddlesden-Popper oxides as OER catalysts, such as $La_{1.7}Ca_{0.3}Ni_{0.75}Cu_{0.25}O_4$ and $LaSr_3Fe_3O_{10}$ [20, 21]. Similarly, the HER catalysis has been done using some Ruddlesden-Popper oxides, such as Sr_2RuO_4 [22]. Several factors have been investigated in an effort to achieve enhanced catalytic activity in these materials, such as A-site cation substitution in $Sr_{2.6}La_{0.4}Fe_2O_7$ [23], nanostructuring in $La_2NiO_{4+\delta}$ particles [24], variation of dimensionality (n) in $La_{n+1}Ni_nO_{3n+1}$ [25], and composite/nanohybrid formation in $NiO–(La_{0.613}Ca_{0.387})_2NiO_{3.562}$ [26]. While Ruddlesden-Popper materials exhibiting either OER or HER activity have been studied earlier, bifunctional RPs that can catalyze both reactions are less common.

Following our recent work on oxide electrocatalysts for OER and HER [3, 27–32], in this article we demonstrate bifunctional electrocatalytic activity in oxygen-deficient RP oxides, $Sr_3Mn_2O_6$, and Sr_3FeMnO_6. Structural studies on similar systems, $Sr_3Mn_2O_{7-\delta}$ [33] and $Sr_3FeMnO_{7-\delta}$ [34], have been reported, where the degree of oxygen deficiency is lower (δ = 0–0.5). In our work, the careful control of synthesis conditions using inert atmosphere has resulted in a greater degree of oxygen-deficiency, to form $Sr_3Mn_2O_6$ and Sr_3FeMnO_6, similar to the previously reported materials $Sr_3Co_2O_6$ [35] and $Sr_3Fe_2O_6$ [16]. In addition, we show the significant enhancement of electrocatalytic activity toward both OER and HER for Sr_3FeMnO_6 as compared to $Sr_3Mn_2O_6$. The observation of bifunctional electrocatalytic properties for Sr_3FeMnO_6 is remarkable.

Experimental

Both materials, $Sr_3Mn_2O_6$ and Sr_3FeMnO_6, were synthesized using the solid state synthesis method in argon atmosphere. The powders of precursor compounds $SrCO_3$ (Aldrich, 99.9%), Fe_2O_3 (Alfa Aesar, 99.998%), and Mn_2O_3 (Alfa Aesar, 99.7%) were mixed and ground together using an agate mortar and pestle. The mixture was pressed into a pellet and heated in argon at 1250 °C for 24 h. The samples were allowed to cool down to room temperature under argon and were reground immediately after being removed from the furnace and refired under the same conditions, in argon at 1250 °C for 24 h, to ensure the formation of pure products. The heating and cooling rates were 100 °C/h in all cases. For comparison, Sr_3FeMnO_7 was also synthesized by a similar method, i.e., two heating runs at 1200 °C for 24 h each, but in air and using MnO_2 as manganese precursor. The structures of products were determined by powder X-ray diffraction using Cu Kα1 radiation (λ = 1.54056 Å). The GSAS software [36] with EXPEGUI interface [37] was used for Rietveld refinements. High-resolution field-emission scanning electron microscopy (SEM) was used to study the microstructure of the materials. Iodometric titrations were performed under an argon atmosphere as reported earlier [38–40], by dissolving about 50 mg of the sample and excess KI (~2 g) in 100 mL of 1 M HCl. A total of 5 mL of the solution was then pipetted out into a conical flask with 20 mL of water. The solution was titrated against 0.025 M $Na_2S_2O_3$. Near the endpoint of the titration, 0.2 mL of a starch solution was added to act as an indicator. The iodometric titrations were done on three different samples for each compound, and the measurement on each sample was repeated three times to ensure reproducibility. Electrocatalytic activities were measured in a three-electrode electrochemical workstation. The working electrode was prepared by the dropcast method for which the catalyst ink was prepared as described previously [31, 41, 42], by mixing 35 mg of the sample with 20 μL of nafion and 7 mg of carbon black. Then, 7 mL of THF was added and stirred for few minutes, followed by sonication for 5 min. The catalyst ink

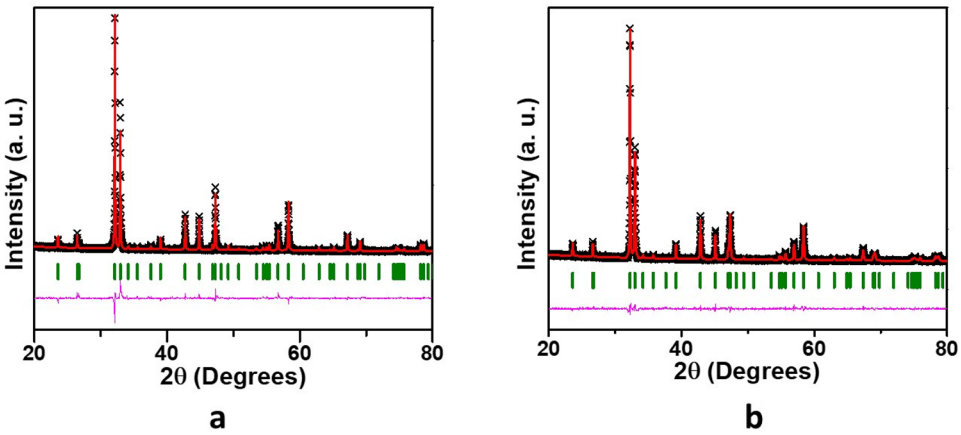

Fig. 2 Rietveld refinement profile for powder X-ray diffraction data of **a** $Sr_3Mn_2O_6$ and **b** Sr_3FeMnO_6. Black crosses, red line, vertical green tick marks, and lower magenta line represent experimental data, the model, peak positions, and difference plot, respectively

(4 coats of 10 µL each) was loaded onto a glassy carbon electrode (GCE) with a diameter of 5 mm (area = 0.196 cm^2) and was dried in air for 24 h. Before starting each measurement, the KOH electrolyte was purged by argon for at least 30 min. The GCE coated with catalyst ink and an Ag/AgCl electrode were used as working and reference electrodes, respectively. The counter electrode was a platinum electrode for OER and a graphite electrode for HER. Potentiostatic electrochemical impedance spectroscopy in the frequency range of 100 kHz to 1 Hz was used to record the resistance (R) before each electrocatalytic experiment. Then, iR-corrected potential was converted to the potential versus reversible hydrogen electrode (RHE) according to the Nernst equation: $E_{RHE} = E_{Ag/AgCl} + 0.059\ pH + E^{\circ}_{Ag/AgCl}$.

Here, $E^{\circ}_{Ag/AgCl} = 0.21$ V for 3 M NaCl and 0.197 V for saturated KCl, used for OER and HER measurements, respectively. The stability tests of catalysts were performed using chronopotentiometry. A two-electrode setup was used for chronopotentiometry, as described in the literature [43]. Briefly, the electrodes were fabricated by loading 100 µL of the catalyst ink, described above, on a 1-cm^2 nickel foam and dried overnight to obtain a total mass loading of ~ 1 mg/cm^2. Two Ni foam electrodes connected to gold leads and gold wires were sandwiched together and separated by a glass fiber filter paper to prevent short-circuiting and crossover. X-ray photoelectron spectroscopy (XPS) data were obtained at room temperature using Al Kα radiation (1486.7 eV).

Results and discussion

Structural characterization

Since both materials were synthesized under argon atmosphere using oxides of trivalent manganese and iron, the ideal formulas should be $Sr_3Mn_2O_6$ and Sr_3FeMnO_6, to maintain the charge neutrality. Iodometric titrations were used to reliably determine the oxygen content. These experiments indicate oxygen stoichiometries of $Sr_3Mn_2O_{6.04(2)}$ and $Sr_3FeMnO_{5.96(2)}$. Rietveld refinements using powder X-ray diffraction data show that the two materials are isostructural and have a tetragonal structure with space group *I4/mmm*, similar to that reported for several analogous oxygen-deficient Ruddlesden-Popper systems, such as $Sr_3Co_2O_6$ [35], $Sr_3Fe_2O_6$ [16], and $La_{1.9}Ca_{1.1}Cu_2O_6$ [44].

Figure 2 shows the Rietveld refinement profiles for both compounds, and Tables 1 and 2 list the refined structural parameters. Compared to a typical Ruddlesden-Popper structure (Fig. 1b) that has the general formula $A_3B_2O_7$, these two materials feature an oxygen-deficiency (Fig. 1a), leading to the formula $A_3B_2O_6$. A typical Ruddlesden-Popper structure with *I4/mmm* space group has oxygen atoms on three crystallographic sites, 0,½,z; 0,0,z; and 0,0,0. In oxygen-deficient systems, the latter site is commonly vacant or partially occupied [16, 35, 44, 45]. As a consequence of this, the coordination geometry around Fe

Table 1 Refined structural parameters for $Sr_3Mn_2O_6$ using powder X-ray diffraction data. Space group: *I4/mmm*, a = 3.84393 (8) Å, b = 3.84393 (8) Å, c = 20.2105 (5) Å, Rp = 0.0558, wRp = 0.0785, $\chi^2 = 2.589$

Elements	x	y	z	Uiso	Occupancy	Multiplicity
Sr1	0.0	0.0	0.5	0.021 (2)	1	2
Sr2	0.0	0.0	0.3153 (2)	0.036 (2)	1	4
Mn1	0.0	0.0	0.0996 (3)	0.013 (2)	1	4
O1	0.0	0.5	0.1011 (7)	0.035 (3)	1	8
O2	0.0	0.0	0.1884 (9)	0.035 (3)	1	4

Table 2 Refined structural parameters for Sr_3FeMnO_6 using powder X-ray diffraction data. Space group: *I4/mmm*, a = 3.8446 (4) Å, b = 3.8446 (4) Å, c = 20.123 (2) Å, Rp = 0.0399, wRp = 0.0512, $\chi^2 = 1.596$

Elements	x	y	z	Uiso	Occupancy	Multiplicity
Sr1	0.0	0.0	0.5	0.036 (2)	1	2
Sr2	0.0	0.0	0.3177 (2)	0.027 (2)	1	4
Fe1	0.0	0.0	0.1005 (2)	0.015 (2)	0.5	4
Mn1	0.0	0.0	0.1005 (2)	0.015 (2)	0.5	4
O1	0.0	0.5	0.0910 (8)	0.087 (9)	1	8
O2	0.0	0.0	0.193 (1)	0.087 (9)	1	4

and Mn changes from octahedral to square-pyramidal. This leads to 2-dimensional layers of corner-sharing (Fe/Mn)O_5 square-pyramids, which alternate in orientation and are separated by Sr atoms (orange spheres in Fig. 1a).

Scanning electron microscopy (SEM) was used to investigate the microstructure of both materials. As observed in Fig. 3, the SEM micrographs show that grain sizes are larger for Sr_3FeMnO_6 as compared with those of $Sr_3Mn_2O_6$.

Electrocatalytic activity for hydrogen-evolution reaction

The electrocatalytic activity for hydrogen-evolution reaction (HER) was studied for both compounds in 1 M KOH, as commonly utilized for HER [46, 47]. The onset potential and the overpotential at 10 mA/cm^2 are the two most important parameters for evaluation of the electrocatalytic activity

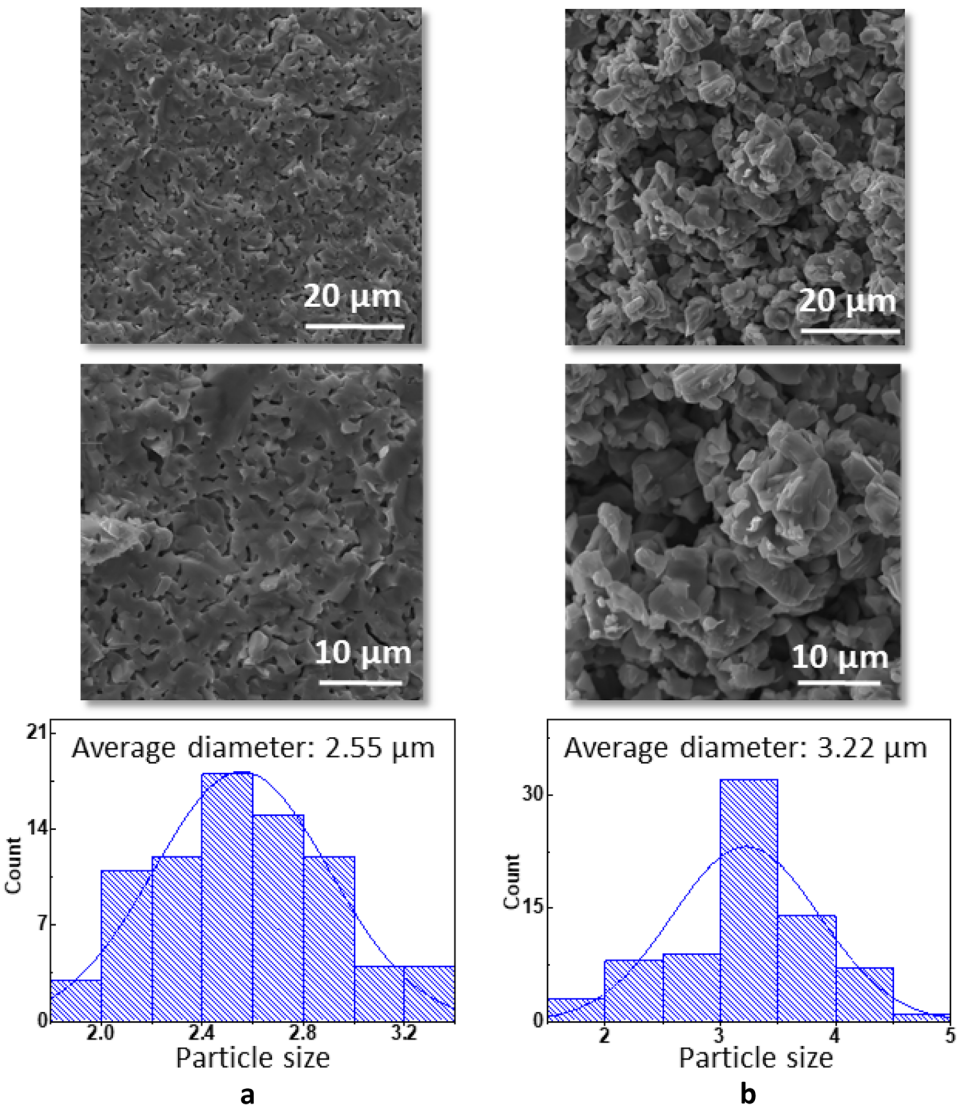

Fig. 3 Scanning electron microscopy images for **a** $Sr_3Mn_2O_6$ and **b** Sr_3FeMnO_6

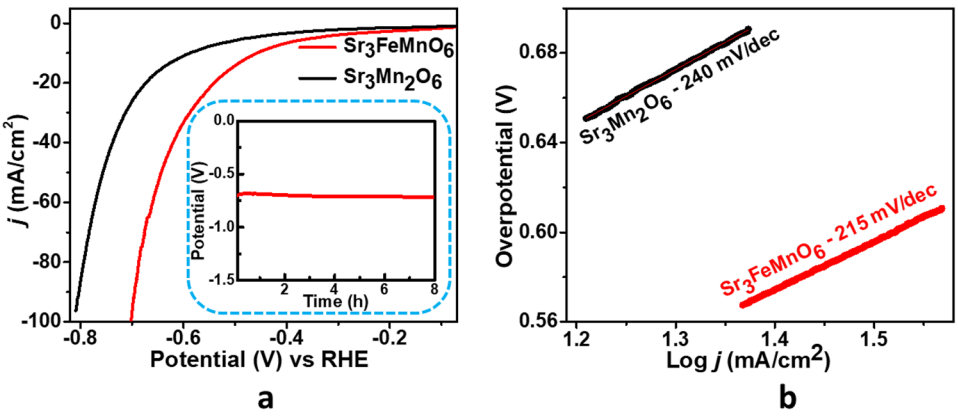

Fig. 4 **a** HER polarization curves in 1 M KOH. The inset shows chronopotentiometry data for Sr_3FeMnO_6. **b** The Tafel plot showing Tafel slopes for both compounds

for HER during heterogeneous catalysis [48–50]. The onset potential corresponds to the start of the Faradaic process, where a rise of current begins. An onset potential of almost 0.0 V versus RHE is observed for the benchmark Pt/C (20 wt. % Pt) catalyst [51, 52]. The HER polarization curves of $Sr_3Mn_2O_6$ and Sr_3FeMnO_6 are shown in Fig. 4a, where the respective onset potential values of ~ − 0.38 V and − 0.30 V are observed. Similarly, the corresponding overpotential (η_{10}) values are − 0.59 V and − 0.45 V at − 10 mA/cm^2 (Fig. 4a) for both catalysts. The best performing catalyst, Sr_3FeMnO_6, is also very stable, as shown by the chronopotentiometry data in the inset of Fig. 4a. While there are some oxide, such as $PrBaCo_2O_{5+\delta}$ (η_{10} = − 0.356 V) [53] and $CaSrFeMnO_{6-\delta}$ (η_{10} = − 0.39 V) [29] which show better catalytic performance, the overpotential values of the catalysts in this work are better than those of some other oxide catalysts in alkaline electrolyte, such as the perovskite oxide $Ba(Fe_{0.7}Ta_{0.3})O_{3-\delta}$ (η_{10} = ~ − 0.70 V) [54].

The evaluation of the reaction kinetics is done using Tafel slopes. The Tafel equation, $\eta = a + b \log j$ (where η is overpotential and j is current density), is utilized to determine the Tafel slope from the linear fit to the plot of η versus log j (Fig. 4b), where the data from the curved region of the polarization curve are considered [30, 55, 56]. We note that the cathodic and anodic scans in polarization curves of these materials are very close to each other. Nevertheless, the average of both scans is commonly used for evaluation of the electrocatalytic activity [19, 41, 57–59]. Faster electron transfer during the HER process is indicated by a smaller value of the Tafel slope. As shown in Fig. 4b, Tafel slopes for $Sr_3Mn_2O_6$ and Sr_3FeMnO_6 are determined to be 240 mV/dec and 215 mV/dec, respectively. These are in the same range as the values reported for some other HER catalysts, such as $MgCr_2O_4$ (217.51 mV/dec) [60] and CuO (243 mV/dec) [61]. The smaller Tafel slope for Sr_3FeMnO_6 compared to that of Sr_3FeMnO_6 indicates faster reaction kinetics and is consistent with the higher electrocatalytic activity of the former material.

Electrocatalytic activity for oxygen-evolution reaction

The electrocatalytic activity for oxygen-evolution reaction (OER) was studied for both compounds in 0.1 M KOH, as commonly used for OER [62–64]. Figure 5a shows the polarization curves from cyclic voltammetry for both materials. Similar to the HER, the onset potential, overpotential at 10 mA cm^{-2}, and Tafel slope were evaluated.

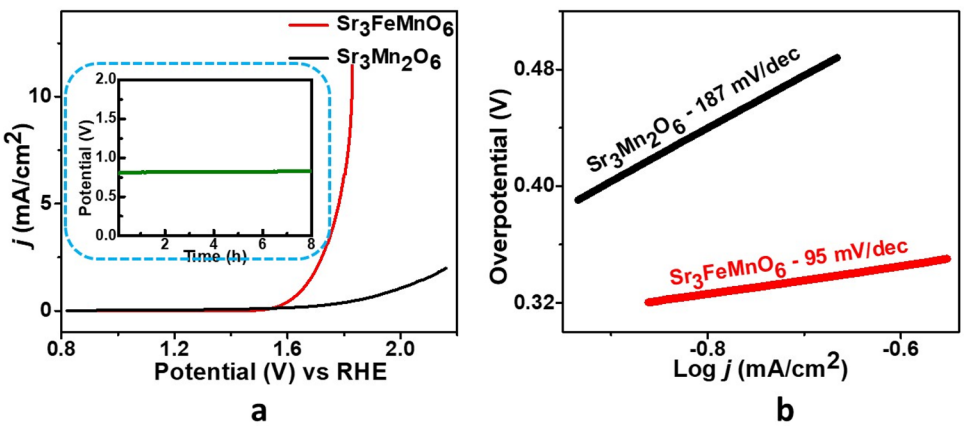

Fig. 5 **a** OER polarization curves in 0.1 M KOH. The inset shows chronopotentiometry data for Sr_3FeMnO_6. **b** The Tafel plot showing Tafel slopes for both compounds

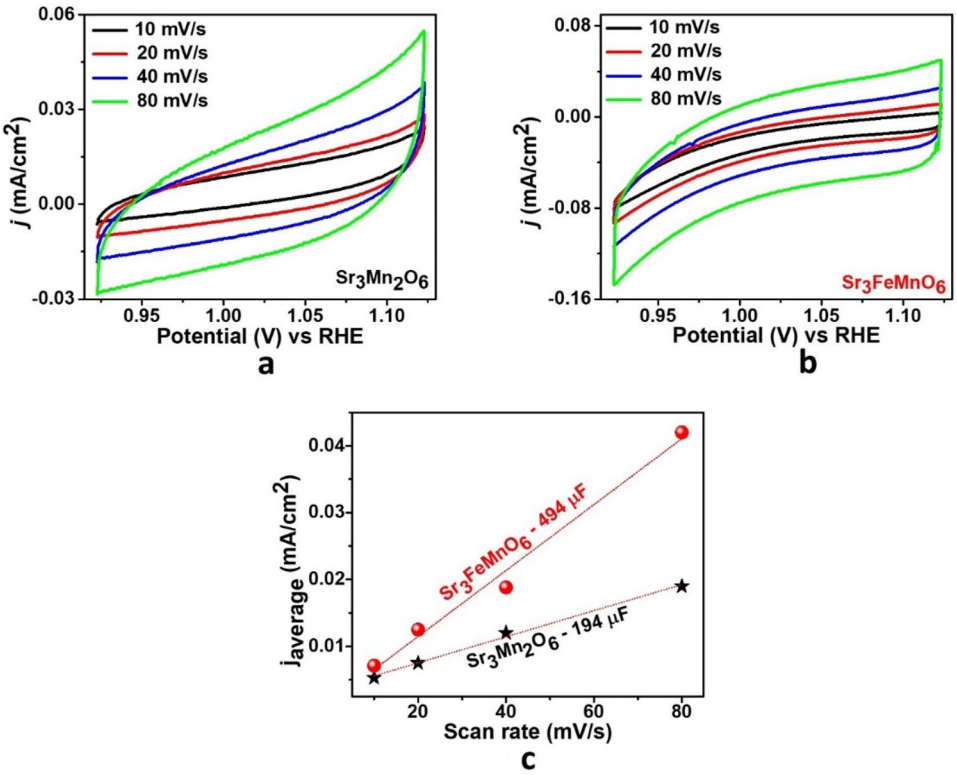

Fig. 6 **a, b** Cyclic voltammetry data in the non-Faradaic region in 1 M KOH. **c** Plot of $j_{average}$ versus scan rate. The double-layer capacitance (C_{dl}) is obtained as the slope of the line of best fit

The corresponding onset potentials for Sr_3FeMnO_6 and $Sr_3Mn_2O_6$ are 1.51 V and 1.63 V, respectively. The onset potential of Sr_3FeMnO_6 is close to that of the well-known OER catalyst $Ba_{0.5}Sr_{0.5}Co_{0.8}Fe_{0.2}O_{6-\delta}$ (BSCF), ~1.5 V [65, 66]. The OER overpotential (η_{10}) is evaluated as the potential, beyond the ideal 1.23 V, which is needed to deliver

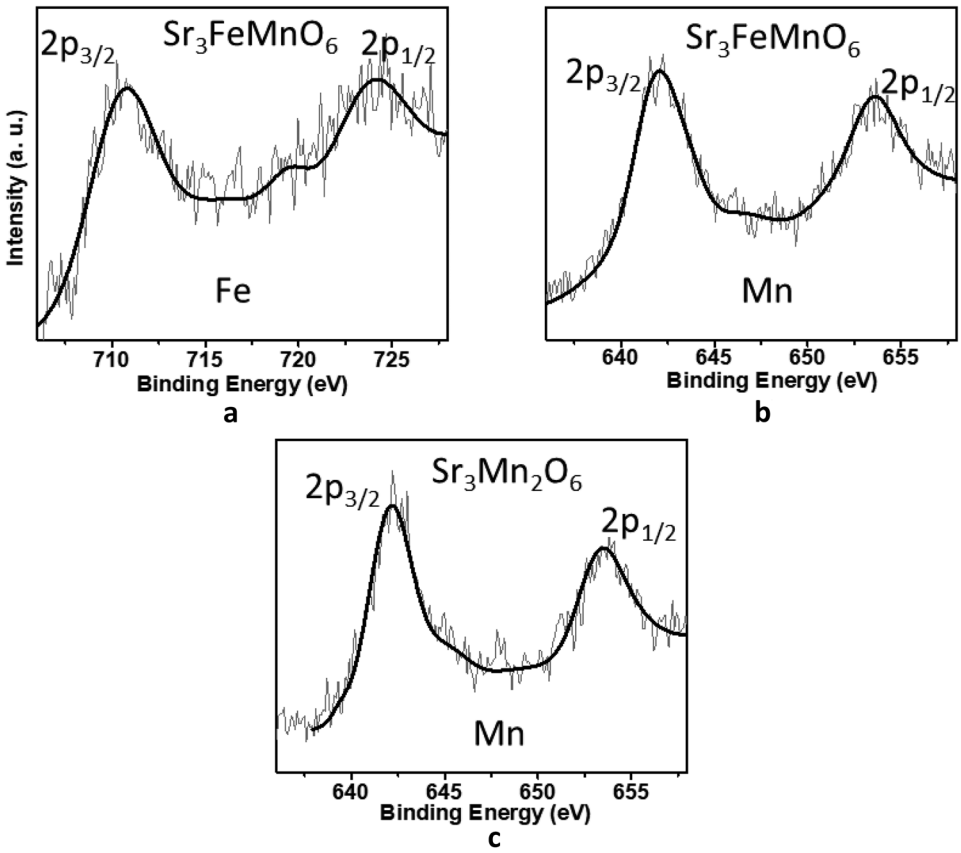

Fig. 7 X-ray photo electron spectroscopy data. **a** and **b** show the Fe and Mn spectra for Sr_3FeMnO_6, and **c** shows the Mn spectrum for $Sr_3Mn_2O_6$

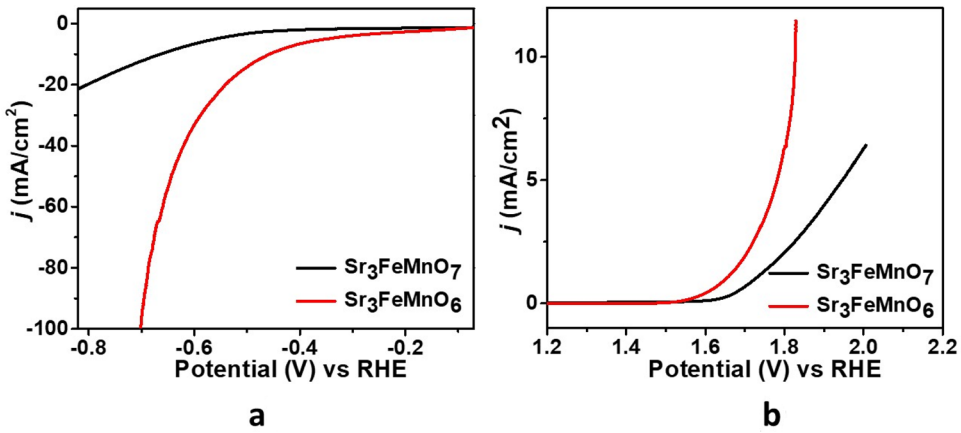

Fig. 8 Comparison of **a** HER and **b** OER activity of $Sr3FeMnO_6$ with the parent compound $Sr3FeMnO_7$

the current density of 10 $mAcm^{-2}$ [67, 68]. Sr_3FeMnO_6 has an overpotential of $\eta_{10}=0.59$ V vs RHE, while the data from $Sr_3Mn_2O_6$ does not even reach the current density of 10 mA cm^{-2} (Fig. 5a). The overpotential of Sr_3FeMnO_6 is not as low as some other electrocatalysts, such as RuO_2 ($\eta_{10}=0.42$ V) [69] and BSCF ($\eta_{10}=0.51$ V) [70]. However, it is comparable to those of several other oxide catalysts, such as $CoFe_2O_4$ ($\eta_{10}=0.59$ V), Co_3O_4 ($\eta_{10}=0.60$ V) [71], and $Ca_2FeMnO_{6-\delta}$ ($\eta_{10}=0.56$ V) [29].

The Tafel slopes for OER were obtained from the linear fit of the plot of η versus log j [30, 55, 56] to evaluate the reaction kinetics, which is related to the electron and mass transport [72, 73]. The Tafel slope values of 187 mV/dec and 95 mV/dec (Fig. 5b) were determined for $Sr_3Mn_2O_6$ and Sr_3FeMnO_6, respectively. This is consistent with the enhanced OER activity of the latter material. Moreover, Sr_3FeMnO_6 is very stable under OER conditions, as shown by the chronopotentiometry data in the inset of Fig. 5a.

We have also calculated electrochemically active surface area (ECSA) for these two materials. The ECSA is estimated from double-layer capacitance, C_{dl}, in the non-Faradic region [74]. In this region, the current is considered to originate mainly from the electrical double layer charge and discharge, which does not have an electron transfer contribution [74, 75]. The ESCA is calculated from the relation $ECSA=C_{dl}/C_s$ [74, 76], where C_s is specific capacitance [74, 76]. Therefore, ECSA is directly proportional to C_{dl}. Hence, it is common practice to use the value of C_{dl} as an indication of the magnitude of ECSA [77–79]. The C_{dl} value can be obtained from the equation $C_{dl}=j_{average}/\nu$ [80, 81], where $j_{average}$ is the average of the absolute values of anodic and cathodic current densities in non-Faradic region. The slope of the plot of $j_{average}$ versus ν gives the C_{dl} value.

Figure 6a and b show the CVs in non-Faradic region, measured at the different scan rates of 10, 20, 40, and 80 mV/s, from which double-layer capacitance (C_{dl}) is obtained. Figure 6c shows comparative plots of $j_{average}$ versus ν, which indicate the C_{dl} values of 494 µF for Sr_3FeMnO_6 and 194 µF for $Sr_3Mn_2O_6$. This is consistent with the greater electrocatalytic activity of the former material, which also showed lower values of overpotential and faster Tafel kinetics compared to the latter compound.

It is possible that the enhanced electrocatalytic properties of Sr_3FeMnO_6 compared with $Sr_3Mn_2O_6$ are related to the electronegativity effect, given the significantly greater electronegativity of Fe relative to Mn. It has been shown previously that the increase in electronegativity results in the lowering of the energy of *d* orbitals [82]. The lowering of the metal *d*-band in oxides can result in an improvement of the overlap between metal *d* and oxygen *p* bands, leading to enhanced covalency and hybridization [83, 84], which serve to boost the electrocatalytic activity [83, 84].

Additionally, the XPS data (Fig. 7) are consistent with trivalent Fe and Mn for both compounds, in line with previous reports [85, 86]. This is expected, given the oxygen stoichiometry, i.e., 6 oxygen per formula unit, obtained from iodometric titrations. To highlight the effect of the oxygen stoichiometry, we conducted further HER and OER experiments using Sr_3FeMnO_7, which is a Ruddlesden-Popper system without oxygen-deficiency. The activity of Sr_3FeMnO_7 is compared with Sr_3FeMnO_6 in Fig. 8, indicating the enhanced performance of the latter due to the presence of oxygen-deficiency.

Conclusions

The 2-dimensional oxides $Sr_3Mn_2O_6$ and Sr_3FeMnO_6 have been synthesized and their structural and electrocatalytic properties have been investigated. Their structures consist of square-pyramidal $(Fe/Mn)O_5$ units that form 2D layers, separated by strontium ions. There is a persistent enhancement of electrocatalytic properties for Sr_3FeMnO_6 as compared to $Sr_3Mn_2O_6$. The former shows enhanced activity toward both OER and HER, exhibiting improved overpotential, Tafel kinetics, and electrochemically active surface area. The

significantly enhanced electrocatalytic performance is attributed to the effect of electronegativity, given the considerably higher electronegativity of Fe compared with Mn, which can lead to the lowering of the *d*-band energy, resulting in better overlap with oxygen *p* bands.

Acknowledgements This work is supported by the National Science Foundation (NSF) under grant no. DMR-1943085.

References

1. Yu N, Jiang G, Liu T, Chen X, Miao M, Zhang Y, Wang Y (2021) Sustain Energy fuels 5:401–411
2. Karki SB, Hona RK, Ramezanipour F (2020) J Electron Mater 49:1557–1567
3. Hona RK, Ramezanipour F (2020) Inorg Chem 59:4685–4692
4. Kananke-Gamage CCW, Ramezanipour F (2021) Dalton Trans 50:14196–14206
5. Adler SB (2004) Chem Rev 104:4791–4844
6. Voorhoeve RJH, Johnson DW, Remeika JP, Gallagher PK (1977) Science 195:827
7. Hodges JP, Jorgensen JD, Xiong X, Dabrowski B, Mini SM, Kimball CW (2000) D Mater Sci U Northern Illinois J. Solid State Chem 151, 209
8. Berenov AV, Atkinson A, Kilner JA, Bucher E, Sitte W (2010) Solid State Ionics 181:819–826
9. Adler SB (1998) Solid State Ionics 111:125–134
10. Xu X, Pan Y, Zhong Y, Ran R, Shao Z (2020) Mater Horiz 7:2519–2565
11. Ruddlesden SN, Popper P (1957) Acta Cryst 10:538–539
12. Ruddlesden SN, Popper P (1958) Acta Cryst 11:54–55
13. Alom MS, Ramezanipour F (2021) Mater Lett 295:129859
14. Beppu K, Hosokawa S, Teramura K, Tanaka T (2015) J Mater Chem A 3:13540–13545
15. Mitchell JF, Millburn JE, Medarde M, Short S, Jorgensen JD, Fernández-Díaz MT (1998) J Solid State Chem 141:599–603
16. Dann SE, Weller MT, Currie DB (1992) J Solid State Chem 97:179–185
17. Gong M, Li Y, Wang H, Liang Y, Wu JZ, Zhou J, Wang J, Regier T, Wei F, Dai H (2013) J Am Chem Soc 135:8452–8455
18. Suntivich J, Gasteiger HA, Yabuuchi N, Nakanishi H, Goodenough JB, Shao-Horn Y (2011) Nat Chem 3:546
19. Suntivich J, May KJ, Gasteiger HA, Goodenough JB, Shao-Horn Y (2011) Science 334:1383
20. Jung K-N, Lee J-I, Im WB, Yoon S, Shin K-H, Lee J-W (2012) Chem Commun 48:9406–9408
21. Takeguchi T, Yamanaka T, Takahashi H, Watanabe H, Kuroki T, Nakanishi H, Orikasa Y, Uchimoto Y, Takano H, Ohguri N, Matsuda M, Murota T, Uosaki K, Ueda W (2013) J Am Chem Soc 135:11125–11130
22. Zhu Y, Tahini HA, Hu Z, Dai J, Chen Y, Sun H, Zhou W, Liu M, Smith SC, Wang H, Shao Z (2019) Nat Commun 10:149
23. Takashima T, Ishikawa K, Irie H (2014) ECS Trans 61:35–41
24. Wei Z, Cui Y, Huang K, Ouyang J, Wu J, Baker AP, Zhang X (2016) RSC Adv 6:17430–17437
25. Yu J, Sunarso J, Zhu Y, Xu X, Ran R, Zhou W, Shao Z (2016) Chem Eur J 22:2719–2727
26. Liu R, Liang F, Zhou W, Yang Y, Zhu Z (2015) Nano Energy 12:115–122
27. Karki SB, Andriotis AN, Menon M, Ramezanipour F, Appl ACS (2021) Energy Mater 4:12063–12066
28. Alom MS, Ramezanipour F (2021) ChemCatChem 13:3510–3516
29. Hona RK, Karki SB, Ramezanipour F, Susttain ACS (2020) Chem Eng 8:11549–11557
30. Karki SB, Ramezanipour F, Appl ACS (2020) Energy Mater 3:10983–10992
31. Hona RK, Ramezanipour F (2019) Angew Chem 58:2060–2063
32. Hona RK, Karki SB, Cao T, Mishra R, Sterbinsky GE, Ramezanipour F (2021) ACS Catal 11:14605–14614
33. Guedes I, Mitchell JF, Argyriou D, Grimsditch M (2000) Phys Rev B 62:13809–13811
34. Song M-S, Kim S-Y, Lee J-Y (2004) Ceramics – Silikáty 48:175–179
35. Dann SE, Weller MT (1995) J Solid State Chem 115:499–507
36. Larson AC, Von Dreele RB (1994), 86–748
37. Toby BH (2001) J Appl Crystallogr 34:210–213
38. Hona RK, Ramezanipour F (2018) J. Mater Sci Mater Electron
39. Hona RK, Ramezanipour F (2019) Polyhedron 167:69–74
40. Karki SB, Ramezanipour F (2019) Mater Today Chem 13:25–33
41. Retuerto M, Pascual L, Calle-Vallejo F, Ferrer P, Gianolio D, Pereira AG, García Á, Torrero J, Fernández-Díaz MT, Bencok P, Peña MA, Fierro JLG, Rojas S (2019) Nat Commun 10:2041
42. Zhou W, Sunarso J (2013) J Phys Chem Lett 4:2982–2988
43. Wang J, Gao Y, Chen D, Liu J, Zhang Z, Shao Z, Ciucci F (2018) ACS Catal 8:364–371
44. Cava RJ, Santoro A, Krajewski JJ, Fleming RM, Waszczak JV, Peck WF, Marsh P (1990) Physica C Supercond 172:138–142
45. Itoh M, Shikano M, Kawaji H, Nakamura T (1991) Solid State Commun 80:545–548
46. Wu A, Gu Y, Xie Y, Tian C, Yan H, Wang D, Zhang X, Cai Z, Fu H, Appl ACS (2019) Mater Interfaces 11:25986–25995
47. Jiang L, Ji S-J, Xue H-G, Suen N-T (2020) Int J Hydrog Energy 45:17533–17539
48. Hwang BJ, Chen HC, Mai FD, Tsai HY, Yang CP, Rick J, Liu YC (2015) Sci Rep 5:16263
49. Mohammed-Ibrahim J, Sun X (2019) J Energy Chem 34:111–160
50. McCrory CCL, Jung S, Ferrer IM, Chatman SM, Peters JC, Jaramillo TF (2015) J Am Chem Soc 137:4347–4357
51. Zhu Y, Zhou W, Zhong Y, Bu Y, Chen X, Zhong Q, Liu M, Shao Z (2017) Adv Energy Mater 7:1602122
52. Xu X, Chen Y, Zhou W, Zhu Z, Su C, Liu M, Shao Z (2016) Adv Mater 28:6442–6448
53. Sun Q, Dai Z, Zhang Z, Chen Z, Lin H, Gao Y, Chen D (2019) J Power sources 427:194–200
54. Ramana CV, Bandi M, Nair AN, Manciu FS, Sreenivasan S, Shutthanandan V, Appl ACS (2021) Energy Mater 4:1313–1322
55. Allen LRF, Bard J (2000) Electrochemical methods: fundamentals and applications, 2nd illustrated ed., Wiley
56. Shinagawa T, Garcia-Esparza AT, Takanabe K (2015) Sci Rep 5:13801–13801
57. Ma Z, Zhang Y, Liu S, Xu W, Wu L, Hsieh Y-C, Liu P, Zhu Y, Sasaki K, Renner JN, Ayers KE, Adzic RR, Wang JX (2018) J Electroanal Chem 819:296–305
58. Baeumer C, Li J, Lu Q, Liang AY-L, Jin L, Martins HP, Duchoň T, Glöß M, Gericke SM, Wohlgemuth MA, Giesen M, Penn EE, Dittmann R, Gunkel F, Waser R, Bajdich M, Nemšák S, Mefford JT, Chueh WC (2021) Nat Mater 20:674–682
59. Retuerto M, Calle-Vallejo F, Pascual L, Lumbeeck G, Fernandez-Diaz MT, Croft M, Gopalakrishnan J, Peña MA, Hadermann J, Greenblatt M, Rojas S, Appl ACS (2019) Mater Interfaces 11:21454–21464
60. Maitra S, Mitra R, Nath TK (2021) J Alloys Compd 858:157679
61. Tahira A, Ibupoto ZH, Willander M, Nur O (2019) Int J Hydrog Energy 44:26148–26157
62. Kumar N, Kumar M, Nagaiah TC, Siruguri V, Rayaprol S, Yadav AK, Jha SN, Bhattacharyya D, Paul AK, Appl ACS (2020) Mater Interfaces 12:9190–9200

63. Xu W, Apodaca N, Wang H, Yan L, Chen G, Zhou M, Ding D, Choudhury P, Luo H (2019) ACS Catal 9:5074–5083
64. Grimaud A, May KJ, Carlton CE, Lee Y-L, Risch M, Hong WT, Zhou J, Shao-Horn Y (2013) Nat Commun 4:2439
65. Chen G, Zhou W, Guan D, Sunarso J, Zhu Y, Hu X, Zhang W, Shao Z (2017) Sci Adv 3:e1603206
66. Chaitoglou S, Bertran E (2017) J Mater Sci 52:8348–8356
67. Wei C, Rao RR, Peng J, Huang B, Stephens IEL, Risch M, Xu ZJ, Shao-Horn Y (2019) Adv Mater 31:1806296
68. Suen N-T, Hung S-F, Quan Q, Zhang N, Xu Y-J, Chen HM (2017) Chem Soc Rev 46:337–365
69. Dong C, Yuan X, Wang X, Liu X, Dong W, Wang R, Duan Y, Huang F (2016) J Mater Chem A 4:11292–11298
70. Zhu Y, Zhou W, Chen Z-G, Chen Y, Su C, Tadé MO, Shao Z (2015) Angew Chem 54:3897–3901
71. Li M, Xiong Y, Liu X, Bo X, Zhang Y, Han C, Guo L (2015) Nanoscale 7:8920–8930
72. Song F, Hu X (2014) J Am Chem Soc 136:16481–16484
73. Moir J, Soheilnia N, O'Brien P, Jelle A, Grozea CM, Faulkner D, Helander MG, Ozin GA (2013) ACS Nano 7:4261–4274
74. Jung S, McCrory CCL, Ferrer IM, Peters JC, Jaramillo TF (2016) J Mater Chem A 4:3068–3076
75. Lu B, Cao D, Wang P, Wang G, Gao Y (2011) Int J Hydrogen energy 36:72–78
76. Oh S, Kim H, Kwon Y, Kim M, Cho E, Kwon H (2016) J Mater Chem A 4:18272–18277
77. Connor P, Schuch J, Kaiser B, Jaegermann W, Phys Z (2020) Chem 234:979–994
78. Pan Y, Chen Y, Li X, Liu Y, Liu C (2015) RSC Adv 5:104740–104749
79. Zhang B, Lui YH, Zhou L, Tang X, Hu S (2017) J Mater Chem A 5:13329–13335
80. Zhu Y, Zhou W, Sunarso J, Zhong Y, Shao Z (2016) Adv funct mater 26:5862–5872
81. Petrie JR, Cooper VR, Freeland JW, Meyer TL, Zhang Z, Lutterman DA, Lee HN (2016) J Am Chem Soc 138:2488–2491
82. Bocquet AE, Mizokawa T, Saitoh T, Namatame H, Fujimori A (1992) Phys Rev B 46:3771–3784
83. Suntivich J, Hong WT, Lee Y-L, Rondinelli JM, Yang W, Goodenough JB, Dabrowski B, Freeland JW, Shao-Horn Y (2014) J Phys Chem C 118:1856–1863
84. Yagi S, Yamada I, Tsukasaki H, Seno A, Murakami M, Fujii H, Chen H, Umezawa N, Abe H, Nishiyama N, Mori S (2015) Nat Commun 6:8249
85. Yamashita T, Hayes P (2008) Appl Surf Sci 254:2441–2449
86. Moulder JF, Stickle WF, Sobol PE, Bomben KD (1992) Handbook of X-Ray Photoelectron Spectroscopy, Editor J. Chastain, Perkin-Elmer Corporation, Eden Prairie